



1 **Homogenized daily sunshine duration over China from 1961 to 2022**

2

3 Yanyi He^{1,3}, Kaicun Wang^{2*}, Kun Yang³, Chunlüe Zhou^{1*}, Changkun Shao³, and Changjian Yin²

4

5 ¹ School of Geography and Planning, Sun Yat-sen University, 510275 Guangzhou, China

6 ² Institute of Carbon Neutrality, Sino-French Institute for Earth System Science, College of
7 Urban and Environmental Sciences, Peking University, 100081 Beijing, China

8 ³ Department of Earth System Science, Ministry of Education Key Laboratory for Earth System
9 Modeling, Institute for Global Change Studies, Tsinghua University, 100084 Beijing, China

10

11 ***Corresponding Author:** Kaicun Wang, kcwang@pku.edu.cn; Chunlüe Zhou,
12 zhouchunlue@mail.sysu.edu.cn

13

14

15



16 **Abstract**

17 Inhomogeneities in the sunshine duration (SSD) observational series, caused by non-climatic
18 factors like China's widespread transition from manual to automatic SSD recorders in 2019 or
19 station relocations, have hindered accurate estimate of near-surface solar radiation for the
20 analysis of global dimming and brightening as well as related applications, such as solar energy
21 planning and agriculture management. This study compiled raw SSD observational data from
22 1961 to 2022 at more than 2,200 stations in China and clearly found that the improved precision
23 from 0.1 hour to 1 minute following the instrument update in 2019 led to a sudden reduction
24 in the frequency of zero SSD from 2019 onwards, referred to as the day0-type discontinuity.
25 For the first time, we systematically corrected this known day0-type discontinuity at 378
26 stations (17%) in China, resulting in an SSD series with comparable frequencies of zero value
27 before and after 2019. On this base, we constructed a homogenization procedure to detect and
28 adjust discontinuities in both the variance and mean of daily SSD from 1961 to 2022. Results
29 show that a total of 1,363 (60%) stations experienced breakpoints in SSD, of which ~65% were
30 confirmed by station relocations and instrument replacements. Compared to the raw SSD, the
31 homogenized SSD is more continuous to the naked eye for various periods, and presents
32 weakened dimming across China from 1961 to 1990 but a non-significant positive trend by a
33 reduction of 60% in the Tibetan Plateau, suggesting that the homogenized SSD tends to better
34 capture the dimming phenomenon. The northern regions continue dimming from 1991 to 2022
35 but the southern regions of China brighten slightly. The implementation of the Action Plan for
36 Air Pollution Prevention and Control since 2013 has contributed to a reversal of SSD trend
37 thereafter, which is better reflected in the homogenized SSD with a trend shift from -0.02 to
38 0.07 hours·day⁻¹/decade from 2013 to 2022 in China, especially in heavily polluted regions.
39 Besides, the relationships of cloud cover fraction and aerosol optical depth with SSD are
40 intensified in the homogenized dataset. These results highlight the importance of the
41 homogenized SSD in accurately understanding the dimming and brightening phenomena. The
42 homogenized SSD dataset is publicly available for community use at
43 <https://doi.org/10.11888/Atmos.tpd.301478> (He et al., 2024).



44 1. Introduction

45 Sunshine duration (SSD) is one of the indispensable observation indicators in ground-
46 based meteorological measurements, capturing the duration of direct sunlight reaching the
47 Earth's surface (Wild et al., 2009; He et al., 2018). As an essential reference indicator to explore
48 variations in surface incident solar radiation (R_s), SSD has profound implications for
49 monitoring climate change, weather forecasting, ecosystem management, and solar energy
50 generation (Stanhill and Cohen, 2003; Baumgartner et al., 2018). Therefore, making high-
51 quality homogenized SSD data publicly accessible to diverse industries is crucial for research,
52 decision-making, and planning across various sectors.

53 SSD measurement dates back 170 years ago, when the sum of sub-periods for which direct
54 solar radiation exceeds 120 W/m^2 was defined as SSD (WMO, 2014). SSD measurements can
55 be broadly categorized into manual and automatic SSD recorders according to the need of
56 human supervision (Wang et al., 2021). The commonly used manual SSD recorders include the
57 Campbell-Stokes sunshine recorder and the Jordan sunshine recorder (Baumgartner et al.,
58 2018). These instruments operate by focusing direct solar radiation onto the photosensitized
59 paper, which burns and leaves one or more continuous traces that represents one or multiple
60 subperiods of sunshine duration (Che et al., 2005; Zhao et al., 2010). SSD is calculated as the
61 sum of the subperiods of the burn within a calendar day. Automatic sunshine recorders employ
62 sensors for observations and the types are diverse, including pyrheliometer, pyranometer,
63 photovoltaic sunshine recorders, and more (Lv et al., 2015).

64 Since the 1950s, the Jordan sunshine recorder has been the primary instrument for
65 measuring SSD in most meteorological stations in China. As reported, only 18 stations in the
66 Heilongjiang Province of Northeast China utilized the Campbell-Stokes sunshine recorder that
67 was subsequently replaced by the Jordan sunshine recorder in 2012 (Lu et al., 2012). In 2019,
68 China carried out a widespread replacement of the Jordan sunshine recorders transitioning to
69 the photoelectric digital SSD recorders at more than 2,400 stations to achieve the automation
70 of SSD measurement (Wang et al., 2020). In the first half of 2019, parallel observations were
71 conducted using both instruments, but starting from the second half of the year, only automatic
72 sunshine recorders were used to record SSD. Compared to traditional manual methods,



73 automatic sunshine recorders have higher precision and automation (Wang et al., 2020).

74 Recent studies have compared parallel observations for the two measurements at some
75 stations for certain regions of China (Lv et al., 2015; Hu et al., 2019; Lu et al., 2019; Lang et
76 al., 2021; Zhou et al., 2021b; Dai et al., 2022). They reported a relatively strong consistency
77 between both observations, but a certain degree of discrepancies still remain, which is closely
78 tied to the position of the sun and varying weather conditions: 1) the photoelectric digital
79 recorders tend to record higher values during weak direct radiation at sunrise and sunset and
80 lower values during strong noon radiation, compared to manual observations; and 2) under
81 persistently sunny weather, the more sensitive photoelectric digital recorders have slightly
82 longer SSD than the manual recorders, but the manual recorders under cloudy conditions with
83 intermittent sunshine tend to register artificially higher values due to lower instrument accuracy
84 and the spot effect.

85 Despite the absence of a sensitivity drift issue in SSD observations by manual sunshine
86 recorders, attributed to the daily replacement of photosensitized paper (Sanchez-Lorenzo and
87 Wild, 2012), the observational data still face challenges in ensuring consistency due to the
88 subjectivity introduced by different observers in practice. On the other hand, due to the
89 limitations of current observation technology, the photoelectric digital SSD recorders also have
90 shortcomings, such as narrow spectral response range, high sensitivity to nearby environment,
91 complex instrument maintenance, and instrument sensitivity drift and difficulty in calibration
92 (Wang et al., 2015; Wang et al., 2021). Several studies have confirmed that the replacement of
93 instruments can lead to non-climatic shifts in SSD and also applied a homogenization to SSD
94 in Iberian Peninsula (Sanchez-Lorenzo et al., 2007), Switzerland (Sanchez-Lorenzo and Wild,
95 2012), Italy (Manara et al., 2015), and Japan (Ma et al., 2022). Besides, other non-climatic
96 factors such as station relocations could also introduce some systematic errors in SSD.

97 Taking into account the aforementioned issues in SSD observations, it is imperative to
98 detect and adjust the discontinuities of SSD series in China, especially in the presence of
99 artificial errors caused by changes in observing instruments, station locations, nearby
100 environmental conditions, observing procedures, or other factors. To achieve this, this study
101 compiled raw SSD data and systematically corrected the known day0-type discontinuity, as



102 described in Section 2.1-2.2. In Section 2.3, a homogenization procedure was described to
103 detect and adjust series discontinuities in the variance and mean of daily SSD, with establishing
104 a reliable reference series. Section 3.1-3.2 analyzed the detected breakpoints and assessed the
105 impacts of series homogenization on trends across various periods. We further examined the
106 influence of cloud cover and aerosols on SSD variations in China in Section 3.3. This study
107 produced a 62-year (1961-2022) homogenized daily SSD dataset in China, which are publicly
108 accessible to support research on China's dimming and brightening phenomena, to improve the
109 assessment of solar radiation simulations and future projections, and to provide valuable data
110 for various applications such as solar energy layout.

111

112 **2. Data and methods**

113 **2.1 Data**

114 The daily observed SSD at 2,425 meteorological stations from 1961 to 2022 were collected
115 from the China Meteorological Administration (CMA, <http://data.cma.cn/en/>). After screening
116 stations based on data continuity and length, i.e., ≥ 15 days of data per month, ≥ 10 months per
117 year, and ≥ 50 years during the entire period, a total of 2,263 stations were involved in this
118 study. Again, a widespread replacement of instruments across China occurred around 2019,
119 transitioning from dark-tube sunshine recorder to photoelectric digital sunshine recorder (Wang
120 et al., 2020).

121 R_s is highly correlated with SSD, but serious concerns have been raised about the reliability
122 of observational R_s data due to poor spatial representativeness, temporal discontinuity, and the
123 effects of urbanization (Wild et al., 2005; Wang et al., 2014; He et al., 2018). In particular for
124 China, issues related to instrument aging, sensitivity drift, and instrument replacements have
125 notably contributed to spurious variations in R_s observations at ~ 100 stations (He and Wang,
126 2020). Therefore, R_s series from nearby stations are insufficient to serve as reference series
127 during homogenization due to their sparse distribution and data inhomogeneity. Reanalysis
128 products have dynamically consistent and spatiotemporally complete atmospheric fields with
129 high resolution and open access of data, addressing these limitations of R_s observations (Zhou



130 et al., 2017). Among these reanalysis products, ERA5 has been verified to outperform in R_s
131 simulations across hourly, daily, monthly, interannual, and decadal scales in China (He et al.,
132 2021; Li et al., 2023). Leveraging the ERA5 R_s data
133 (<https://cds.climate.copernicus.eu/cdsapp#!/dataset/reanalysis-era5-single-levels>), we
134 estimated sunshine duration based on the criteria of hourly direct R_s exceeding 120 W/m^2 that
135 is consistent with instrument measurements (He et al., 2018), to serve as a reference series for
136 homogenizing the observational SSD data. Meanwhile, SSD estimate from hourly direct R_s of
137 MERRA2 data from 1980 to 2022 (<https://gmao.gsfc.nasa.gov/reanalysis/MERRA-2/>) was
138 used as an aid in constructing the reference series.

139 To examine the effects of cloud and aerosol on SSD variations, daily cloud cover fraction
140 (CCF) and aerosol optical depth at 550nm (AOD) from 2003 to 2022 were obtained from a
141 MODIS product at $1^\circ \times 1^\circ$ grids (MCD06COSP_D3,
142 https://ladsweb.modaps.eosdis.nasa.gov/archive/allData/62/MCD06COSP_D3_MODIS)
143 (Pincus et al., 2012; Swales et al., 2018).

144 According to topography and administrative divisions in China, seven subregions were
145 identified as shown in Figure 1a, i.e., Northwest China (I), the Tibetan Plateau (II), Southwest
146 China (III), Northeast China (IV), North China (V), Southeast China (VI), and the Loess
147 Plateau (VII). A relocation event of station was defined as $\Delta\text{latitude} > 0.01^\circ$, $\Delta\text{longitude} >$
148 0.01° , or $\Delta\text{altitude} > 10\text{m}$ before and after a specific date. The history of station relocations in
149 China is reflected by the number of relocations in Figure 1a, and the fraction of the stations
150 with relocations from 1961 to 2022 in Figure 1b. The average of the number of relocations in
151 China is about 4 (Fig. 1a). The instrument replacements in 2019 are accompanied with changes
152 of the measurement height, presenting the unusually frequent relocations at the time (Fig. 1b).

153 2.2 Correction of known day0-type discontinuity

154 Following the update of automatic sunshine recorders around 2019, which improved
155 measurement precision from 0.1 hour to 1 minute (Lang et al., 2021), we observed a sudden
156 reduction in the frequency of zero SSD at specific stations in China after 2019. In most
157 instances, raw daily SSD is absent of a value of zero for more than six consecutive months,



158 which is significantly different from series pattern observed prior to 2019. We identified the
159 segments with this known day0-type discontinuity that characterized by more than six
160 consecutive months of non-zero SSD.

161 Results show that the day0-type discontinuity occurs almost in one segment per station,
162 totaling 378 stations (i.e., 17% of stations in China) distributed mainly across northern China,
163 Tibetan Plateau, and part of Southwest China (Fig. 2a), and is concentrated in 2019 to 2020
164 (Fig. 2b). Note that the improved precision may not lead to a notable day0-type discontinuity
165 in some regions or such minor discontinuities may not be easily identifiable. The spatial
166 distribution of discontinuities and the years of their most frequent occurrence align with the
167 update of automatic sunshine recorders in 2019 or later, as well as with station relocations
168 (Figs. 1 vs 2). We employed the quantile-matching (QM) algorithm to correct the segments
169 with the identified day0-type discontinuities by utilizing the longest segment that is free of the
170 discontinuity, which produced the SSD0 series for the subsequent homogenization. The
171 magnitude of correction reaches up to $-5 \text{ hours}\cdot\text{day}^{-1}$ at two example stations in Northeast
172 China and Northwest China, respectively (Fig. 3a and 3d). After correction, the frequency of
173 low values, especially zero values, has increased visibly in 2019 or later in the SSD0 series
174 compared to the raw SSD series, and then is comparable to the frequency before 2019 (Fig. 3b
175 and 3e). The monthly SSD0 anomaly after correction appears to be more continuous (Fig. 3c
176 and 3f). Note that the mean shift of the segment after 2020 like at station No. 51627 (Fig. 3f)
177 would be statistically homogenized in the following sections.

178 **2.3 Homogenization procedure**

179 Since parallel observations for the photoelectric digital SSD recorder and manual SSD
180 recorder are not publicly available, we are unable to directly explore the relationship between
181 the two datasets. Data series homogenization offers us with an effective way to address
182 discontinuities in climate time series caused by non-climatic factors like station relocation and
183 instrument replacements. Much effort has been devoted to develop homogenization methods,
184 such as the standard normal homogeneity test (SNHT) (Alexandersson, 1986), two-phase
185 regression-based methods (Solow, 1987), Bayesian-based methods (Perreault et al., 2000; Chu
186 and Zhao, 2004), penalized maximal T test (PMT) (Wang et al., 2007), and penalized maximal



187 *F* test (PMF) (Wang, 2008a). Reeves et al. (2007) compared these methods and argued that
188 SNH test may work best when trend and periodic effects are diminished by using homogeneous
189 reference series. However, Wang et al. (2007) and Wang (2008a) pointed out that unequal
190 sample sizes affect the false alarm rate and detection power of SNHT-type tests. They
191 demonstrated that PMT and PMF tests with incorporating penalized empirical corrections offer
192 higher detection power and are suited for long-term series with significant climate trends
193 (Wang, 2008b; Wang et al., 2010). Since their release, PMT and PMF tests have been
194 successfully applied to various climate elements including temperature, precipitation,
195 humidity, wind speed, and R_s (Wang et al., 2010; Dai et al., 2011; Domonkos, 2011; Yang et
196 al., 2018; Zhou et al., 2018; Ma et al., 2022; Zhou et al., 2022), making them the chosen
197 methods for this study.

198 During the homogenization, a well-established reference series is essential for sufficiently
199 detecting and adjusting inhomogeneities in long-term climate time series, since it can help
200 remove most real climate changes and synoptic variations (i.e., noise), thereby improving the
201 signal-to-noise ratio of discontinuities and enabling statistical detection and removal of
202 spurious shifts (Dai et al., 2011; Zhou et al., 2022). In this study, we first established a reliable
203 reference series to account for background weather and climate variations, and then detected
204 and adjusted spurious breakpoints in the mean and variance of the non-zero daily SSD0 series
205 using the well-established ERA5 reference series, resulting in a homogenized daily SSD
206 observational dataset.

207 **2.3.1 Construction of the reference series**

208 A reliable reference series should effectively capture most background weather and climate
209 variations while remaining homogeneous. ERA5 SSD series is highly correlated with the SSD0
210 series on daily and monthly time scales across China (Fig. 4a and 4d), which ensures that ERA5
211 SSD as a reference series can remove most background weather and climate variations from
212 the SSD0 series, thereby facilitating the detection of breakpoints.

213 Previous studies have indicated that ERA5 significantly overestimates the variation in R_s
214 from 2003 to 2010 in China (He et al., 2021; Shao et al., 2022). This overestimation is inherited
215 in the SSD estimated from hourly direct R_s of ERA5, presenting inhomogeneities during this



216 period, particular in North China and Southeast China (Fig. 5). We evaluated several reanalysis
217 products and found that the SSD estimated from hourly direct R_s of MERRA2 does not suffer
218 from this issue (Fig. 5), maybe since MERRA2 assimilates space-based observations of
219 aerosols and improves R_s simulations in China to some extent (Feng and Wang, 2021).
220 Meanwhile, MERRA2 SSD is also highly correlated with the SSD0 series (Fig. 4b and 4e). To
221 mitigate the discontinuity of ERA5 SSD from 2003 to 2010, we took MERRA2 SSD as the
222 reference series and applied the PMT test to detect breakpoints in the monthly ERA5 SSD
223 series. After obtaining the breakpoints, we employed the QM algorithm to adjust discontinuities
224 in the daily ERA5 SSD series, using the longest segment as the reference. Results show that
225 the homogenized ERA5 SSD not only exhibits higher correlations with the SSD0 series on
226 daily and monthly time scales (Fig. 4c and 4f), but also greatly alleviated the overestimation
227 from 2003 to 2010 (Fig. 5), which makes it a suitable reference series for the subsequent
228 homogenization.

229 2.3.2 Detection and adjustment of breakpoints in non-zero daily SSD0 series

230 Zero values in a daily meteorological series should remain unaltered unless supported by
231 evidence or reports of trace occurrence or changes in measuring precision (Wang et al., 2010).
232 After the known day0-type discontinuity has been corrected in Section 2.2 above, the
233 subsequent homogenization was performed on the variance and mean of non-zero daily SSD0
234 series. To achieve this, we decomposed the non-zero daily SSD0 series into two components:
235 intramonthly and monthly.

236 Firstly, we applied an improved Kolmogorov–Smirnov (K-S) test (Dai et al., 2011; Zhou
237 et al., 2021a) at a 99.9% significance level to the intramonthly component of the daily
238 difference series ($DSSD_{\text{intra}}$) for detecting breakpoints in the variance of the non-zero daily
239 SSD0 series:

$$240 \quad DSSD_{\text{intra}} = SSD_{\text{aobs}} - \alpha \cdot SSD_{\text{aERA5}} \quad (1)$$

$$241 \quad SSD_{\text{aobs}} = SSD_{\text{dobs}} - SSD_{\text{mobs}} \quad (2)$$

$$242 \quad SSD_{\text{aERA5}} = SSD_{\text{dERA5}} - SSD_{\text{mERA5}} \quad (3)$$

243 where SSD_{dobs} and SSD_{dERA5} are the non-zero daily values of SSD0 and homogenized ERA5



244 SSD; $SSD_{m_{obs}}$ and $SSD_{m_{ERA5}}$ are the monthly mean $SSD_{d_{obs}}$ and $SSD_{d_{ERA5}}$; $SSD_{a_{obs}}$ and
245 $SSD_{a_{ERA5}}$ are the daily anomalies of $SSD_{d_{obs}}$ and $SSD_{d_{ERA5}}$, respectively; α is the liner
246 regression coefficient of $SSD_{a_{obs}}$ against $SSD_{a_{ERA5}}$. Systematic biases in the reanalysis and the
247 effect of the station-versus-grid discrepancies can be greatly eliminated by the regression
248 against the observation.

249 Secondly, we applied both PMT and PMF tests developed by Wang et al. (2007) and Wang
250 (2008b) at a 99% significance level to detect breakpoints in the monthly mean of the non-zero
251 SSD_0 series. The breakpoints detected by both methods within one year were kept. In the PMT
252 test, $SSD_{m_{ERA5}}$ was taken as the input of reference series. Consistently, the monthly difference
253 series ($DSSD_m$) requested in the PMF test was constructed as follows:

$$254 \quad DSSD_m = SSD_{m_{obs}} - \beta \cdot SSD_{m_{ERA5}} \quad (4)$$

255 where β is liner regression coefficient between $SSD_{m_{obs}}$ and $SSD_{m_{ERA5}}$.

256 To obtain a manageable number of breakpoints in the final, we followed the approach of
257 Zhou et al. (2021a) by setting 365 days between breakpoints as the threshold to merge the
258 detected breakpoints above. For cases with three or more breakpoints within 365 days of each
259 other, we retained only the middle breakpoint, and for two breakpoints, we kept the one with
260 the larger test statistic.

261 Finally, we adopted the QM algorithm from Wang et al. (2010) to remove the merged
262 breakpoints in the daily difference series ($DSSD_d$) that is the residual series from the regression
263 (the slope γ) of $SSD_{d_{obs}}$ on $SSD_{d_{ERA5}}$:

$$264 \quad DSSD_d = SSD_{d_{obs}} - \gamma \cdot SSD_{d_{ERA5}} \quad (5)$$

265 This produced a homogenized daily SSD dataset for China, covering the period from 1961 to
266 2022, with zero values backfilled. The longest segment was chosen as the baseline segment
267 primarily due to its relative homogeneity and reliability. Despite the use of advanced automated
268 instruments with higher precision from 2019 onwards, the segment is still too short to fully
269 meet the criteria for a reliable baseline segment. The segment after 2019 will be considered as
270 the baseline segment when the dataset is updated in the coming years.

271



272 3. Results

273 3.1 Detection and adjustment of breakpoints

274 One or two breakpoints in the variance of the $DSSD_{intra}$ series were detected at 328
275 stations, mainly in Northwest China, Northeast China, North China, and the Loess Plateau (Fig.
276 6a). Most of these breakpoints occur around 2019 (Fig. 6a2), coinciding with the instrument
277 replacements from dark-tube sunshine recorder to photoelectric digital sunshine recorder, as
278 well as the station relocations (Fig. 1b). During the period of 1961-2022, 1,238 stations (55%)
279 in China suffered from the breakpoints in the mean of the $DSSD_m$ series (Fig. 6b1). These
280 breakpoints are evenly distributed across China (Fig. 6b1), with many occurring around 2019
281 and two additional small peaks around 1972 and 2003 (Fig. 6b2). Approximately 52% of the
282 stations in China were detected with one breakpoint, 32% with two breakpoints, 12% with three
283 breakpoints, and few stations with more than four breakpoints (Fig. 6b1). After merging the
284 two types of breakpoints above, a total of 1,363 stations experienced breakpoints, accounting
285 for approximately 60% of the stations in China (Fig. 6c1). The merged breakpoints are densely
286 concentrated in northern China, where approximately 71% of the stations are affected, with the
287 highest density (74%) observed on the Loess Plateau, while approximately 47% of the stations
288 are affected in southern China (Fig. 6c1). A higher fraction of stations with breakpoints occurs
289 around 2019 after merging (Fig. 6c2).

290 The detected breakpoints may be associated with factors such as instrument replacements,
291 station relocations, equipment malfunctions, operation errors, and other environment changes,
292 any of which may contribute to data series inhomogeneity (Sanchez-Lorenzo and Wild, 2012;
293 Wang et al., 2020). To empirically demonstrate it, we attempted to collect such types of
294 information but were only able to compile a detailed set of information about station relocation.
295 We found that over 50% of stations in 2019 were relocated (Fig. 1b), mostly because they
296 needed to change their positions or heights due to instrument replacements or urbanization.
297 The hit probability for matching detected breakpoints with stations relocations is
298 approximately 65%. Noted that the breakpoints may be caused by factors other than station
299 relocations, while some station locations may not have resulted in any breakpoints, or certain
300 breakpoints may not have emerged from the background weather or climate variations that was



301 not easily detected by a statistical method.

302 To remove the artificial breakpoints detected above, the QM algorithm was implemented
303 to achieve homogenization by aligning the empirical distributions of all segments. For
304 examples, three breakpoints in the variance and mean of the SSD0 series were detected at
305 Station No. 51627 (Fig. 7). The first two breakpoints are associated with the station relocations
306 and the last breakpoints are related to the replacement of instrument in 2019. The adjustments
307 estimated based on the QM algorithm for the three breakpoints are approximately 1, -0.5, and
308 $2.8 \text{ hours} \cdot \text{day}^{-1}$, respectively (Fig. 7b). After adjustments, the monthly SSD0 anomaly series
309 appears continuous and reasonable, particularly after 2019 (Fig. 7c).

310 **3.2 Comparison of trends before and after homogenization**

311 The discontinuities hidden in the series are bound to affect the estimate of long-term trends
312 of SSD. Fig. 8 shows series comparisons among the raw SSD, SSD0, and homogenized SSD
313 averaged over China and its seven subregions. The most significant adjustments are evident in
314 2019 or later, occurring across China (Fig. 8). This is jointly resulted from two aspects: the
315 high robustness of dark-tube sunshine recorder in measuring SSD before 2019, and the
316 widespread switch to photoelectric digital sunshine recorder in 2019 that caused notable shifts
317 compared to earlier period. Based on the periods of dimming and brightening in China revealed
318 by prior researches (He et al., 2018; He and Wang, 2020), trend analysis was conducted for two
319 major periods: 1961-1990 and 1991-2022.

320 During the period of 1961-1990, the homogenized SSD exhibits a significant downward
321 trend of $-0.11 \text{ hours} \cdot \text{day}^{-1}/\text{decade}$ ($p < 0.05$) in China, compared to a slightly steeper decline of
322 $-0.13 \text{ hours} \cdot \text{day}^{-1}/\text{decade}$ ($p < 0.05$) in the raw SSD (Figs. 8-9 and Table 1), though the difference
323 between the two is not evident. After homogenization, the dimming of homogenized SSD
324 weakens across China except the Tibetan Plateau, with the most pronounced weakening in
325 North China by $0.04 \text{ hours} \cdot \text{day}^{-1}/\text{decade}$ compared to the raw SSD (Figs. 8-9 and Table 1).
326 Meanwhile, the Tibetan Plateau shows a reduced and non-significant increase in the
327 homogenized SSD ($0.02 \text{ hours} \cdot \text{day}^{-1}/\text{decade}$ with a reduction of 60%, $p > 0.10$) compared to the
328 raw SSD ($0.05 \text{ hours} \cdot \text{day}^{-1}/\text{decade}$, $p < 0.10$) during the dimming period of China (i.e., 1961 to
329 1990) (Figs. 8-9 and Table 1), suggesting that the homogenized SSD tends to better describe



330 the dimming phenomenon.

331 During the period of 1991-2022, only the southern regions of China experienced slight
332 brightening, whereas the northern regions continued dimming (Fig. 9). The national average
333 SSD trend of China remains unchanged before and after homogenization, with a decline of
334 about $-0.04 \text{ hours}\cdot\text{day}^{-1}/\text{decade}$ ($p<0.10$) (Table 1). However, the magnitudes of decadal trends
335 change significantly across various regions. In heavily polluted regions such as North China
336 and the Loess Plateau, the degree of dimming diminishes in homogenized SSD. Specifically,
337 the SSD trend decreases from $-0.14 \text{ hours}\cdot\text{day}^{-1}/\text{decade}$ ($p<0.05$) to $-0.12 \text{ hours}\cdot\text{day}^{-1}/\text{decade}$
338 ($p<0.05$) in North China, and from $-0.11 \text{ hours}\cdot\text{day}^{-1}/\text{decade}$ ($p<0.05$) to $-0.08 \text{ hours}\cdot\text{day}^{-1}/\text{decade}$
339 ($p>0.10$) in the Loess Plateau (Figs. 8-9 and Table 1). In addition, for the Tibetan
340 Plateau and Northeast China, the SSD after homogenization presents a more pronounced
341 decline compared to the raw data (Figs. 8-9 and Table 1).

342 In 2013, China issued and implemented the Air Pollution Prevention and Control Action
343 Plan (APPCAP), to address severe air pollution and its associated health risks. The subsequent
344 strengthening of air quality measures may have contributed to a reversal of SSD trend
345 thereafter. During the period of 2013-2022, the national average SSD in China shifts from a
346 decrease of $-0.02 \text{ hours}\cdot\text{day}^{-1}/\text{decade}$ to an increase of $0.07 \text{ hours}\cdot\text{day}^{-1}/\text{decade}$ after
347 homogenization, reflecting well the effect of the APPCAP implementation on the SSD trend
348 reversal compared to earlier periods (Figs. 8-9 and Table 1). Especially for heavily polluted
349 regions like North China, Southeast China, Loess Plateau, and Northeast China, the
350 homogenized SSD shows more brightening after homogenization, with the most notable
351 increase in North China where the trend increases from $0.16 \text{ hours}\cdot\text{day}^{-1}/\text{decade}$ ($p>0.10$) to $0.42 \text{ hours}\cdot\text{day}^{-1}/\text{decade}$ ($p<0.10$)
352 ($p<0.05$) (Figs. 8-9 and Table 1). Due to the instrument replacement in 2019, the
353 artificial breakpoints in the SSD series have been removed and the homogenized SSD series
354 appear more continuous to the naked eye (Fig. 8b-8e). Specifically, the homogenized SSD has
355 a weakened trend ($-0.16 \text{ hours}\cdot\text{day}^{-1}/\text{decade}$, $p>0.10$) compared to the raw data (-0.52
356 $\text{hours}\cdot\text{day}^{-1}/\text{decade}$, $p<0.05$) in Northwest China. The homogenized SSD declines with -0.36
357 $\text{hours}\cdot\text{day}^{-1}/\text{decade}$ ($p<0.10$) and $-0.16 \text{ hours}\cdot\text{day}^{-1}/\text{decade}$ ($p>0.10$) in the Tibetan Plateau and
358 Southwest China, respectively (Fig. 8b-d). In summary, considering the uncertainties brought



359 by the series inhomogeneities caused by non-climatic factors such as instrument replacements
360 and station relocations, it is very necessary to address these inhomogeneities, particularly in
361 studies focused on detecting and attributing global dimming and brightening.

362 **3.3 Relationships of cloud and aerosol with sunshine duration**

363 Cloud and aerosol affect the amount of solar radiation reaching the Earth's surface through
364 sunlight reflection, absorption, and scattering, making their combined effects on solar radiation
365 a key factor in understanding global dimming and brightening (Wild, 2009; Wild, 2012; Feng
366 and Wang, 2021; Ma et al., 2022). SSD serves as a core indicator of solar radiation, which is
367 modulated by both cloud cover and aerosols. Due to limitations of satellite data, this section
368 focuses on the relationships of cloud cover fraction (CCF) and aerosol optical depth (AOD) on
369 SSD variations solely over the 20-year period starting from 2003.

370 Fig. 10 shows maps of decadal changes in AOD, CCF, and the homogenized SSD, and
371 their time series at the locations collocated with stations in China. For the entire period of 2003-
372 2022, the correlation coefficient of the averaged CCF in China against the raw SSD is -0.53
373 ($p < 0.05$), and its coefficient against the homogenized SSD reaches -0.71 ($p < 0.05$). On the other
374 hand, in the heavily polluted regions such as North China and Northeast China, the correlation
375 coefficient between AOD and SSD is significantly negative, and the relationships are
376 intensified after homogenization, i.e., from -0.40 ($p < 0.10$) to -0.56 ($p < 0.05$) and from -0.41
377 ($p < 0.10$) to -0.54 ($p < 0.10$), respectively. These relationship changes indicate a stronger
378 relationship with CCF and AOD in the homogenized SSD dataset.

379 During the period of 2003-2012, the average SSD in China decreases at a rate of -0.20
380 hours·day⁻¹/decade ($p > 0.10$), accompanied by slight increases in both CCF and AOD (Fig.
381 10g). For regional details, the significant increase of AOD in North China (Fig. 10a) and the
382 significant increase in CCF in Southeast China (Fig. 10b) jointly contributes to regional
383 divergences in the SSD decadal changes of China during this period (Fig. 10c).

384 The effect of the APPCAP implementation on AOD can be clearly seen with a rapid
385 reduction after 2013 (Fig. 10a, 10d, and 10g). CCF also exhibits a corresponding shift from the
386 perspective of spatial distribution of its decadal changes, especially in North China (Fig. 10b



387 vs 10e), maybe due to various cloud-aerosol interactions. These changes of AOD and CCF
388 contributes to the SSD brightening after 2013, which is reflected in the maps and time series
389 of their decadal changes (Fig. 10). During the period of 2013-2022, the spatially coherent
390 pattern of AOD decadal reductions (-0.12 1/decade, $p < 0.05$) inevitably lead to an overall SSD
391 brightening, on the basis of which the spatial detail of CCF decadal changes further inversely
392 shapes the pattern of SSD decadal changes (Fig. 10d-10f). This results in a decadal change of
393 0.07 hours \cdot day $^{-1}$ /decade ($p > 0.10$) in the national average SSD (Fig. 10g). In heavily polluted
394 regions such as North China, it's clear that decreases in both AOD and CCF jointly result in
395 the enhanced brightening in the localized SSD (Fig. 10d-10f).

396

397 **4. Data availability**

398 The homogenized dataset of daily sunshine duration at 2.0×2.0 grids in China from 1961
399 to 2022 generated in this study, provides a valuable database for assessing and attributing solar
400 radiation variations, and will also be a key for various applications in the solar energy industry,
401 agricultural management, and ecology and climatology research. The homogenized dataset is
402 freely accessed via the following link, <https://doi.org/10.11888/Atmos.tpd.301478> (He et al.,
403 2024).

404

405 **5. Conclusions and discussion**

406 Inhomogeneities in climate series, stemming from non-climatic factors such as instrument
407 replacements and station relocations, inevitably affect the estimate of long-term trends. While
408 dark-tube sunshine recorder robustly measured SSD in China prior to 2019, the widespread
409 transition to photoelectric digital sunshine recorder in 2019 introduced significant non-climate
410 discontinuities in SSD. After compiling raw SSD observational data, we first noted a sudden
411 reduction in the frequency of zero SSD in segments from 2019 onwards, attributed to improved
412 measurement precision from 0.1 hour to 1 minute following the instrument update in 2019.
413 This known day0-type discontinuity affected a total of 378 stations (~17% of stations in China),
414 occurring almost in one segment per station, predominantly located in northern China, the



415 Tibetan Plateau, and parts of Southwest China. We applied the quantile-matching algorithm to
416 correct the segments with the day0-type discontinuities, using the longest segment unaffected
417 by the discontinuity, which produced the SSD0 series that has comparable frequencies of zero
418 SSD before and after 2019.

419 To further address the remaining discontinuities, we developed a homogenization
420 procedure for producing a 62-year (1961-2022) homogenized daily SSD dataset in China. First,
421 a well-established ERA5 SSD was constructed as a reliable reference series with the help of
422 MERRA2 SSD to eliminate the background weather and climate variations (i.e., noise) for
423 enhancing the signal-to-noise of artificial discontinuities. Second, two separate steps were
424 taken to statistically detect discontinuities in the variance and mean of the non-zero daily SSD0
425 series. Results show that breakpoints in the variance are mainly concentrated in the northern
426 part of China, while the breakpoints in the mean are evenly distributed across China. After
427 merging the two types of breakpoints above, a total of 1,363 stations experienced breakpoints,
428 accounting for ~60% of the stations in China. The peak in the number of breakpoints occurs in
429 2019, coinciding with the nationwide transition from manual to automated SSD recorders. In
430 all, ~65% of the detected breakpoints were confirmed by station relocations and associated
431 instrument replacements. Finally, the merged breakpoints were removed by the quantile-
432 matching algorithm to produce the final homogenized daily dataset.

433 Compared to the raw SSD, the homogenized SSD shows more continuous variations across
434 various time scales, providing a solid basis for estimating reliable long-term trends for various
435 periods. During the dimming (1961 to 1990), the homogenized SSD presents weakened
436 dimming across China compared to the raw SSD, particularly in the Tibetan Plateau, where the
437 trend shifts from a significantly positive to a non-significant negative with a reduction of 60%,
438 suggesting that the homogenized SSD tends to better describe the dimming phenomenon.
439 During the period of 1991-2022, only the southern regions of China experienced slight
440 brightening, whereas the northern regions continued dimming. In heavily polluted regions such
441 as North China and the Loess Plateau, the extent of dimming diminishes in homogenized SSD.
442 The subsequent strengthening of air quality measures after issuing the APPCAP in 2013 in
443 China may have contributed to a reversal of SSD trend thereafter. During the period of 2013-



444 2022, the national average SSD in China shifts from a decrease of $-0.02 \text{ hours}\cdot\text{day}^{-1}/\text{decade}$ to
445 an increase of $0.07 \text{ hours}\cdot\text{day}^{-1}/\text{decade}$ after homogenization, reflecting well the effect of the
446 APPCAP implementation on the SSD trend reversal compared to earlier periods. Especially in
447 heavily polluted regions, the homogenized SSD shows more brightening after homogenization,
448 with the most notable increase observed in North China.

449 We further examined the regulatory effects of clouds and aerosols on SSD changes using
450 the satellite data from 2003 to 2022. Our analysis reveals that the relationships of CCF and
451 AOD with SSD are intensified in the homogenized dataset. During the period of 2003-2012,
452 the average SSD in China decreases at a rate of $-0.20 \text{ hours}\cdot\text{day}^{-1}/\text{decade}$ ($p>0.10$),
453 accompanied by slight increases in both CCF and AOD. The effect of the APPCAP
454 implementation on AOD is evident, with a rapid reduction in AOD after 2013. In the
455 subsequent period from 2013 to 2022, the spatially coherent pattern of AOD decadal reductions
456 results in an overall SSD brightening, on the basis of which the spatial detail of CCF decadal
457 changes further inversely shapes the pattern of SSD decadal changes. This leads to a national
458 average SSD change of $0.07 \text{ hours}\cdot\text{day}^{-1}/\text{decade}$ ($p>0.10$). These regulatory effects of clouds
459 and aerosols on SSD obtained using only 20-years satellite CCF and AOD data were also
460 confirmed by prior studies regarding R_s . For instances, earlier studies have demonstrated that
461 clouds were only able to explain R_s changes in the southern part of China before 1990, but
462 accounted for changes across the entire China after 1990 (Yang et al., 2013; He and Wang,
463 2020). Wang et al. (2012) suggested that seasonal and interannual variations in R_s are
464 predominantly affected by clouds, while decadal variations are mainly dominated by aerosols.

465 Our long-term homogenized daily SSD dataset not only enables a reliable assessment of
466 global dimming and brightening in China, but also provides valuable insights for planning,
467 designing, and evaluating benefits across various sectors, including solar energy, agriculture,
468 and environmental management. Moreover, the homogenization experience including
469 constructing a reference series with the aid of current atmospheric reanalysis could be adapted
470 to have broader applications in the homogenization of other climate elements or over other
471 regions to develop a global dataset.



472 **Author contributions**

473 YH, KW, and KY designed the research. YH performed the analysis and wrote the draft. CZ
474 advised the homogenization method. KW and CY collected raw SSD observational data and
475 YH compiled all the remaining data. All the authors jointly contributed to interpreting the
476 results and editing the final paper.

477 **Competing interests**

478 The authors have declared no any competing interests.

479

480 **Acknowledgements** This study was supported by the National Natural Science Foundation of
481 China (No. 42205171), the Starting Grant for Introduced Talents of Sun Yat-sen University
482 (37000-12230039), and the Central University Basic Research Business Fee on the Training of
483 Young Teachers (37000-31610006). Sunshine duration and other meteorological observations
484 at 2,425 stations were obtained from the China Meteorological Administration (CMA,
485 <http://data.cma.cn/en>). ERA5 and MEERA2 data were downloaded respectively at
486 <https://www.ecmwf.int/en/forecasts/datasets/reanalysis-datasets/era5> and
487 <https://gmao.gsfc.nasa.gov/reanalysis/MERRA-2/>. MODIS data were downloaded at
488 https://ladsweb.modaps.eosdis.nasa.gov/archive/allData/62/MCD06COSP_D3_MODIS.



489 **References**

- 490 Alexandersson, H.: A homogeneity test applied to precipitation data, *J. Climatol.*, 6, 661-675,
491 1986.
- 492 Baumgartner, D., Pötzi, W., Freislich, H., Strutzmann, H., Veronig, A., Foelsche, U., and Rieder,
493 H.: A comparison of long-term parallel measurements of sunshine duration obtained
494 with a Campbell-Stokes sunshine recorder and two automated sunshine sensors, *Theor.*
495 *Appl. Climatol.*, 133, 263-275, 2018.
- 496 Che, H. Z., Shi, G. Y., Zhang, X. Y., Arimoto, R., Zhao, J. Q., Xu, L., Wang, B., and Chen, Z.
497 H.: Analysis of 40 years of solar radiation data from China, 1961-2000, *Geophys. Res.*
498 *Lett.*, 32, 10.1029/2004gl022322, 2005.
- 499 Chu, P.-S. and Zhao, X.: Bayesian change-point analysis of tropical cyclone activity: The
500 central North Pacific case, *J. Clim.*, 17, 4893-4901, 2004.
- 501 Dai, A. G., Wang, J. H., Thorne, P. W., Parker, D. E., Haimberger, L., and Wang, X. L. L.: A
502 New Approach to Homogenize Daily Radiosonde Humidity Data, *J. Clim.*, 24, 965-991,
503 10.1175/2010jcli3816.1, 2011.
- 504 Dai, H., Huang, S., Wang, Y., and Lai, L.: Analysis and evaluation based on parallel observation
505 data of artificial and automatic sunshine observation in Jiangxi province, *Jiangxi*
506 *Science*, 40, 370-373, 2022.
- 507 Domonkos, P.: Efficiency evaluation for detecting inhomogeneities by objective
508 homogenisation methods, *Theor. Appl. Climatol.*, 105, 455-467, 2011.
- 509 Feng, F. and Wang, K.: Merging ground-based sunshine duration observations with satellite
510 cloud and aerosol retrievals to produce high-resolution long-term surface solar radiation
511 over China, *Earth Syst. Sci. Data*, 13, 907-922, 10.5194/essd-13-907-2021, 2021.
- 512 He, Y. and Wang, K.: Variability in direct and diffuse solar radiation across China from 1958
513 to 2017, *Geophys. Res. Lett.*, 47, e2019GL084570, 10.1029/2019gl084570, 2020.
- 514 He, Y., Wang, K., and Feng, F.: Improvement of ERA5 over ERA-Interim in simulating surface
515 incident solar radiation throughout China, *J. Clim.*, 34, 3853–3867, 2021.
- 516 He, Y., Wang, K. C., Zhou, C. L., and Wild, M.: A revisit of global dimming and brightening
517 based on the sunshine duration, *Geophys. Res. Lett.*, 45, 4281-4289,
518 10.1029/2018gl077424, 2018.
- 519 He, Y., Wang, K., Yang, K., Zhou, C., Shao, C., and Yin, C.: Homogenized daily sunshine
520 duration at 2°×2° over China from 1961 to 2022, National Tibetan Plateau / Third Pole
521 Environment Data Center, <https://doi.org/10.11888/Atmos.tpdc.301478>, 2024.
- 522 Hu, S., Mo, Y., Ding, L., and Wang, Z.: Comparative analysis on the performance of digital
523 sunshine recorder based on photoelectric principle, *Meteorological, Hydrological and*
524 *Marine Instruments*, 4, 23-28, 2019.
- 525 Lang, G., An, C., and Yuan, Q.: Comparison and analysis of sunshine duration between DFC1



- 526 photoelectric digital sunshine recorder and dark-tube sunshine recorder, Mid-low
527 Latitude Mountain Meteorology, 45, 4, 2021.
- 528 Li, Z., Yang, X., and Tang, H.: Evaluation of the hourly ERA5 radiation product and its
529 relationship with aerosols over China, *Atmos. Res.*, 294, 106941,
530 <https://doi.org/10.1016/j.atmosres.2023.106941>, 2023.
- 531 Lu, Z., Yu, S., and Hou, S.: Discussions on measurement uncertainty of sunshine duration by
532 Jordan and Campbell-Stokes sunshine recorders, *Heilongjiang Meteorology*, 29, 31-32,
533 2012.
- 534 Lu, Z., Zhang, Y., Wang, J., Wang, F., and Zhou, Y.: Comparative analysis of manual and
535 automatic sunlight observation data, *Heilongjiang Meteorology*, 36, 31-32, 2019.
- 536 Lv, W., Chong, W., and Ding, L.: Test and analysis on performance comparison of photoelectric
537 automatic sunshine duration recorder, *Journal of Electronic Measurement and
538 Instrument*, 29, 928-933, 2015.
- 539 Ma, Q., Wang, K. C., He, Y. Y., Su, L. Y., Wu, Q. Z., Liu, H., and Zhang, Y. R.: Homogenized
540 century-long surface incident solar radiation over Japan, *Earth Syst. Sci. Data*, 14, 463-
541 477, 10.5194/essd-14-463-2022, 2022.
- 542 Manara, V., Beltrano, M. C., Brunetti, M., Maugeri, M., Sanchez-Lorenzo, A., Simolo, C., and
543 Sorrenti, S.: Sunshine duration variability and trends in Italy from homogenized
544 instrumental time series (1936-2013), *J. Geophys. Res. Atmos.*, 120, 3622-3641,
545 10.1002/2014jd022560, 2015.
- 546 Perreault, L., Bernier, J., Bobée, B., and Parent, E.: Bayesian change-point analysis in
547 hydrometeorological time series. Part 1. The normal model revisited, *J. Hydrol.*, 235,
548 221-241, 2000.
- 549 Pincus, R., Platnick, S., Ackerman, S. A., Hemler, R. S., and Patrick Hofmann, R. J.:
550 Reconciling simulated and observed views of clouds: MODIS, ISCCP, and the limits
551 of instrument simulators, *J. Clim.*, 25, 4699-4720, 2012.
- 552 Reeves, J., Chen, J., Wang, X. L., Lund, R., and Lu, Q. Q.: A review and comparison of
553 changepoint detection techniques for climate data, *J. Appl. Meteorol. Clim.*, 46, 900-
554 915, 2007.
- 555 Sanchez-Lorenzo, A. and Wild, M.: Decadal variations in estimated surface solar radiation over
556 Switzerland since the late 19th century, *Atmos. Chem. Phys.*, 12, 8635-8644,
557 10.5194/acp-12-8635-2012, 2012.
- 558 Sanchez-Lorenzo, A., Brunetti, M., Calbo, J., and Martin-Vide, J.: Recent spatial and temporal
559 variability and trends of sunshine duration over the Iberian Peninsula from a
560 homogenized data set, *J. Geophys. Res. Atmos.*, 112, 10.1029/2007jd008677, 2007.
- 561 Shao, C., Yang, K., Tang, W., He, Y., Jiang, Y., Lu, H., Fu, H., and Zheng, J.: Convolutional
562 neural network-based homogenization for constructing a long-term global surface solar
563 radiation dataset, *Renew. Sust. Energ. Rev.*, 169, 112952,



- 564 <https://doi.org/10.1016/j.rser.2022.112952>, 2022.
- 565 Solow, A. R.: Testing for climate change: An application of the two-phase regression model, J.
566 Climate Appl. Meteorol., 1401-1405, 1987.
- 567 Stanhill, G. and Cohen, S.: Solar radiation changes in the United States during the twentieth
568 century: Evidence from sunshine duration measurements, J. Clim., 18, 1503-1512, 2003.
- 569 Swales, D. J., Pincus, R., and Bodas-Salcedo, A.: The cloud feedback model intercomparison
570 project observational simulator package: Version 2, Geosci. Model Dev., 11, 77-81,
571 2018.
- 572 Wang, K., Dickinson, R. E., Wild, M., and Liang, S.: Atmospheric impacts on climatic
573 variability of surface incident solar radiation, Atmos. Chem. Phys., 12, 9581-9592,
574 10.5194/acp-12-9581-2012, 2012.
- 575 Wang, K., Ma, Q., Li, Z., and Wang, J.: Decadal variability of surface incident solar radiation
576 over China: observations, satellite retrievals, and reanalyses, J. Geophys. Res. Atom.,
577 120, 6500-6514, 10.1002/2015jd023420, 2015.
- 578 Wang, K., Ma, Q., Wang, X., and Wild, M.: Urban impacts on mean and trend of surface
579 incident solar radiation, Geophys. Res. Lett., 41, 4664-4668, 10.1002/2014gl060201,
580 2014.
- 581 Wang, X. L., Wen, Q. H., and Wu, Y.: Penalized maximal t test for detecting undocumented
582 mean change in climate data series, J. Appl. Meteorol. Clim., 46, 916-931, 2007.
- 583 Wang, X. L. L.: Penalized maximal F test for detecting undocumented mean shift without trend
584 change, J. Atmos. Oceanic Technol., 25, 368-384, 10.1175/2007jtecha982.1, 2008a.
- 585 Wang, X. L. L.: Accounting for autocorrelation in detecting mean shifts in climate data series
586 using the penalized maximal t or F test, J. Appl. Meteorol. Clim., 47, 2423-2444,
587 10.1175/2008jamc1741.1, 2008b.
- 588 Wang, X. L. L., Chen, H. F., Wu, Y. H., Feng, Y., and Pu, Q. A.: New Techniques for the
589 Detection and Adjustment of Shifts in Daily Precipitation Data Series, J. Appl. Meteorol.
590 Clim., 49, 2416-2436, 10.1175/2010jamc2376.1, 2010.
- 591 Wang, Y., Zhang, G., Sun, G., Liu, S., and Yang, J.: Research survey and development trend of
592 sunshine recorder, Chinese Journal of Scientific Instrument, 41, 1-14, 2020.
- 593 Wang, Y., Zhang, G., Sun, G., Liu, S., Xu, D., Yang, S., and Wu, L.: A review on sunshine
594 recorders: Evolution of operation principle and construction, Measurement, 186, 110-
595 138, 2021.
- 596 Wild, M.: Global dimming and brightening: A review, J. Geophys. Res. Atom., 114, D00D16,
597 10.1029/2008jd011470, 2009.
- 598 Wild, M.: Enlightening global dimming and brightening, Bull. Am. Meteorol. Soc., 93, 27-37,
599 10.1175/bams-d-11-00074.1, 2012.
- 600 Wild, M., Truessel, B., Ohmura, A., Long, C. N., Koenig-Langlo, G., Dutton, E. G., and

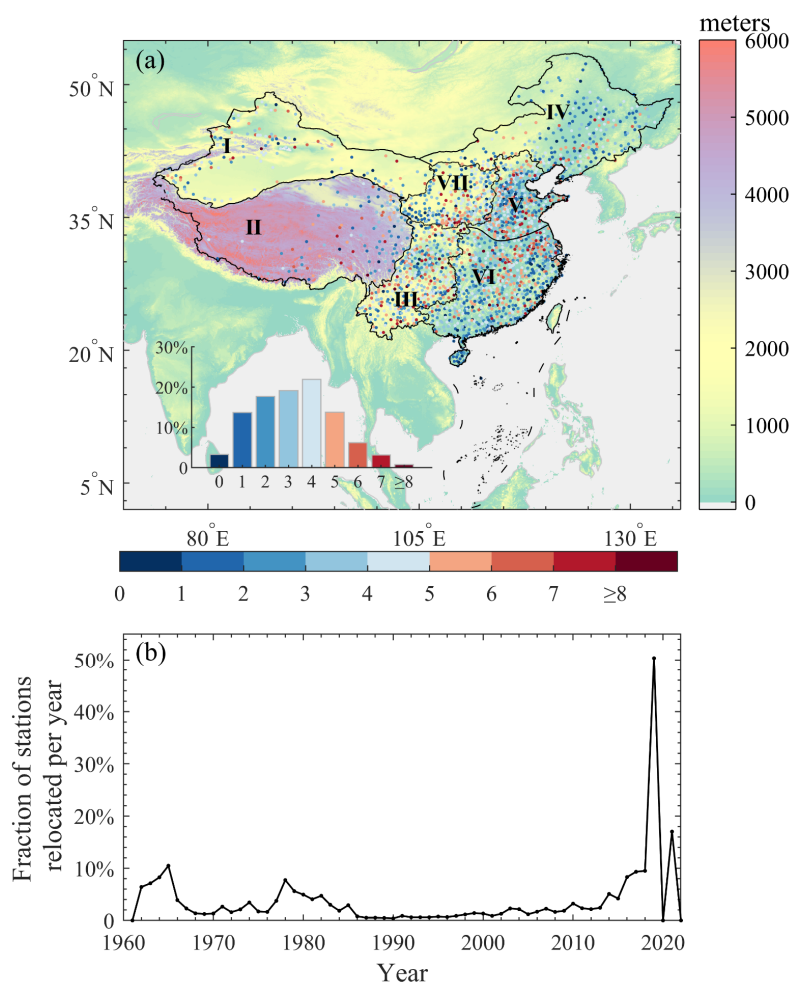


- 601 Tsvetkov, A.: Global dimming and brightening: an update beyond 2000, *J. Geophys.*
602 *Res. Atom.*, 114, D00D13, 10.1029/2008jd011382, 2009.
- 603 Wild, M., Gilgen, H., Roesch, A., Ohmura, A., Long, C. N., Dutton, E. G., Forgan, B., Kallis,
604 A., Russak, V., and Tsvetkov, A.: From dimming to brightening: decadal changes in
605 solar radiation at Earth's surface, *Science*, 308, 847-850, 10.1126/science.1103215,
606 2005.
- 607 WMO: Guide to Meteorological Instruments and Methods of Observation. WMO-No. 8,
608 Secretariat of the WMO, Geneva, 2014.
- 609 Yang, S., Wang, X. L., and Wild, M.: Homogenization and trend analysis of the 1958-2016 in
610 situ surface solar radiation records in China, *J. Clim.*, 31, 4529-4541, 10.1175/jcli-d-
611 17-0891.1, 2018.
- 612 Yang, S., Shi, G., Wang, B., Yang, H., and Duan, Y.: Trends in Surface Solar Radiation (SSR)
613 and the Effect of Clouds on SSR during 1961-2009 in China, *Chinese Journal of*
614 *Atmospheric Sciences*, 37, 963-970, 2013.
- 615 Zhao, D., Luo, Y., Gao, G., Zhu, C., and Shen, Y.: Long-Term Changes and Essential Climatic
616 Characteristics of Sunshine Duration over China during 1961-2007, *Resources Science*,
617 32, 701-711, 2010.
- 618 Zhou, C., He, Y., and Wang, K.: On the suitability of current atmospheric reanalyses for
619 regional warming studies over China, *Atmos. Chem. Phys.*, 18, 8113-8136,
620 10.5194/acp-18-8113-2018, 2018.
- 621 Zhou, C., Wang, K., and Ma, Q.: Evaluation of eight current reanalyses in simulating land
622 surface temperature from 1979 to 2003 in China, *J. Clim.*, 30, 7379-7398, 10.1175/jcli-
623 d-16-0903.1, 2017.
- 624 Zhou, C., Wang, J., Dai, A., and Thorne, P.: A New Approach to Homogenize Global Subdaily
625 Radiosonde Temperature Data from 1958 to 2018, *J. Clim.*, 34, 1163-1183,
626 10.1175/jcli-d-20-0352.1, 2021a.
- 627 Zhou, C., Azorin-Molina, C., Engström, E., Minola, L., Wern, L., Hellström, S., Lönn, J., and
628 Chen, D.: HomogWS-se: a century-long homogenized dataset of near-surface wind
629 speed observations since 1925 rescued in Sweden, *Earth Syst. Sci. Data*, 14, 2167-2177,
630 2022.
- 631 Zhou, H., Quan, W., Wang, Z., Li, X., Li, Y., and Zhao, H.: Comparison of sunshine duration
632 measurements between a Jordan sunshine recorder and three automatic sensors at
633 Shangdianzi GAW station, *J. Meteorol. Res.*, 35, 716-728, 2021b.



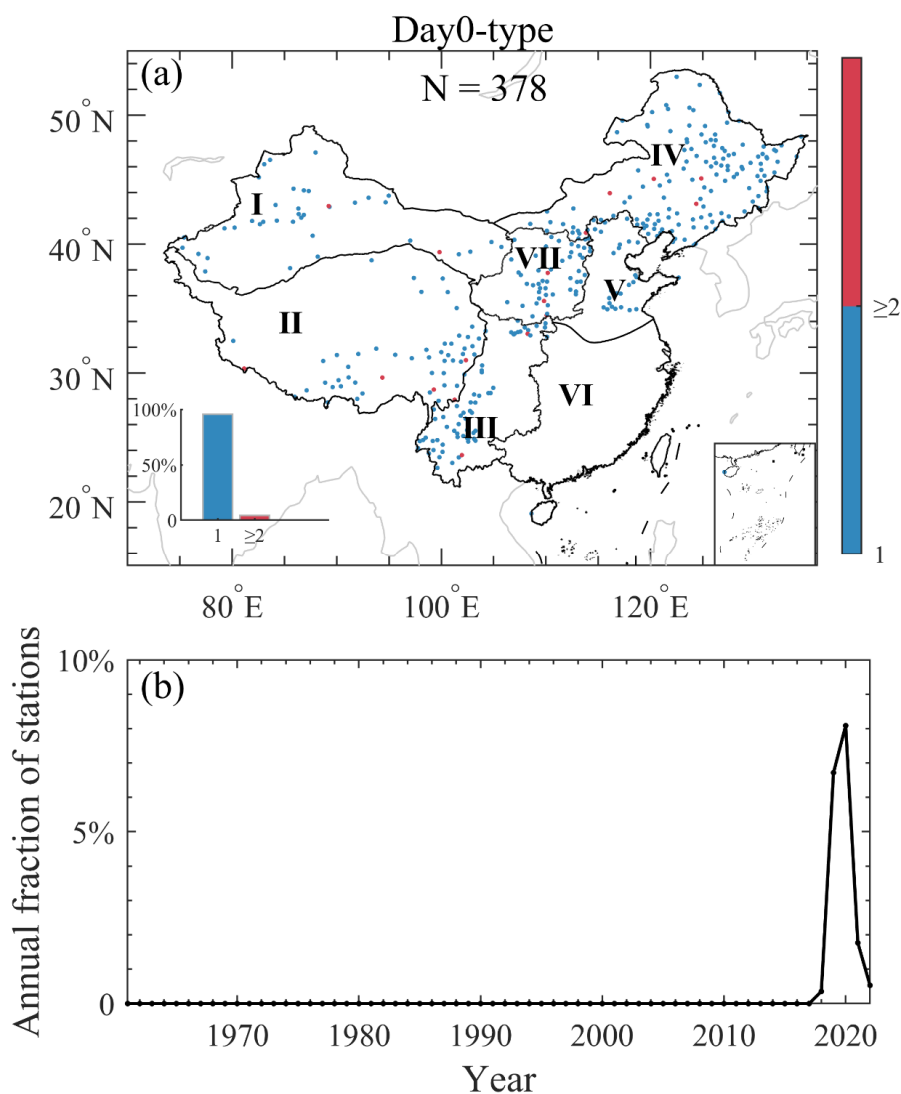
634 **Table 1** Trends of sunshine duration (unit: hours·day⁻¹/decade) before and after
 635 homogenization in China and its seven subregions, i.e., Northwest China (I), Tibetan Plateau
 636 (II), Southwest China (III), Northeast China (IV), North China (V), Southeast China (VI), and
 637 Loess Plateau (VII), during three periods of 1961-1990, 1991-2022, and 2013-2022. Trends
 638 with a significance level of 0.05 are shown in bold, while those with a significance level of 0.1
 639 are italicized.

	1961-1990		1991-2022		2013-2022	
	Before	After	Before	After	Before	After
China	-0.13	-0.11	<i>-0.04</i>	<i>-0.04</i>	-0.02	0.07
Northwest China (I)	-0.04	-0.02	-0.06	-0.03	-0.52	-0.16
Tibet Plateau (II)	<i>0.05</i>	0.02	<i>-0.05</i>	-0.07	-0.20	<i>-0.36</i>
Southwest China (III)	-0.13	-0.11	<i>0.06</i>	0.02	-0.05	-0.16
Northeast China (IV)	-0.11	-0.10	-0.01	-0.02	0.23	0.26
North China (V)	-0.22	-0.18	-0.14	-0.12	0.16	<i>0.42</i>
Southeast China (VI)	-0.23	-0.21	-0.02	-0.02	0.10	0.21
Loess Plateau (VII)	<i>-0.13</i>	-0.11	-0.11	-0.08	-0.08	0.11



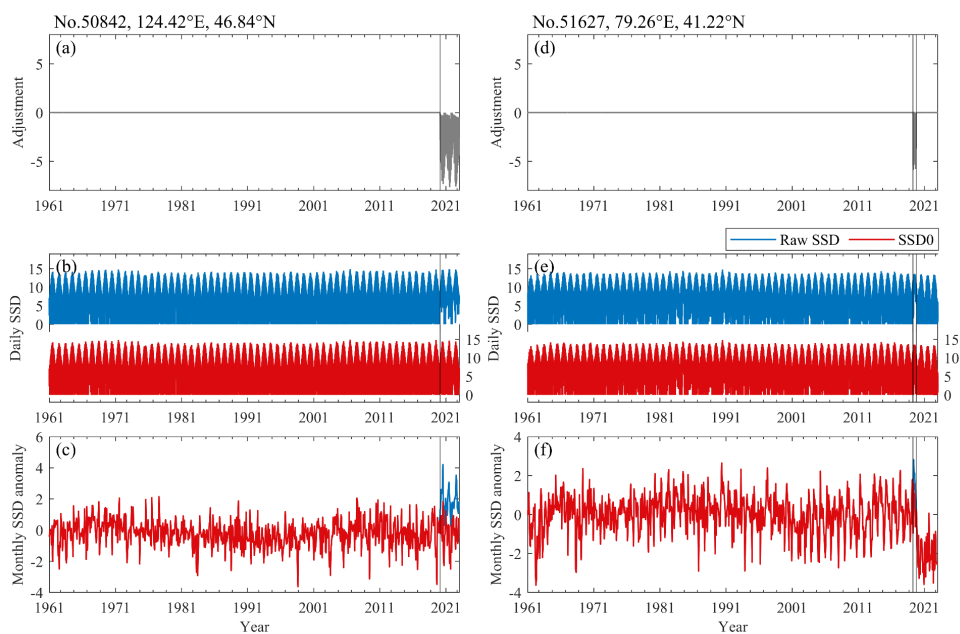
640

641 **Figure 1** (a) Map of the number of relocations for 2,263 national meteorological stations (dots
642 colored by the bottom color bar, unit: times) in China during the period of 1961 to 2022. A
643 relocation event is defined as $\Delta\text{latitude} > 0.01^\circ$, $\Delta\text{longitude} > 0.01^\circ$, or $\Delta\text{altitude} > 10\text{m}$ before
644 and after a specific date. The elevation map serves as the background and is colored by the
645 right-side color bar. The sub-figure in the bottom left illustrates the percentage of stations
646 corresponding to the number of relocations for all stations. According to topography and
647 administrative divisions of China, seven subregions were identified, i.e., Northwest China (I),
648 Tibetan Plateau (II), Southwest China (III), Northeast China (IV), North China (V), Southeast
649 China (VI), and Loess Plateau (VII). (b) Time series of the fraction of stations (unit: %) that
650 underwent one or more relocations per year. The unusually frequent relocations in 2019 were
651 accompanied with the instrument replacements that occurred that year.



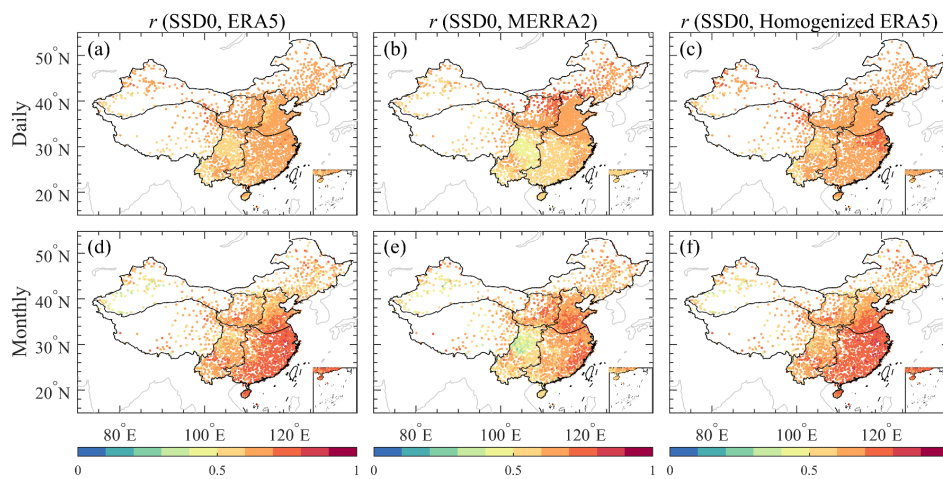
652

653 **Figure 2** (a) Map of stations with the day0-type discontinuities in the monthly count of days
654 with zero sunshine duration. The right-side color bar illustrates the total number of segments
655 with the day0-type discontinuities for each station. The sub-figure in the bottom left shows the
656 percentage of stations with different numbers of such segments per station. A total of 378
657 stations were identified with the day0-type discontinuities. (b) Annual fraction (unit: %) of
658 stations with the day0-type discontinuities from 1961 to 2022.



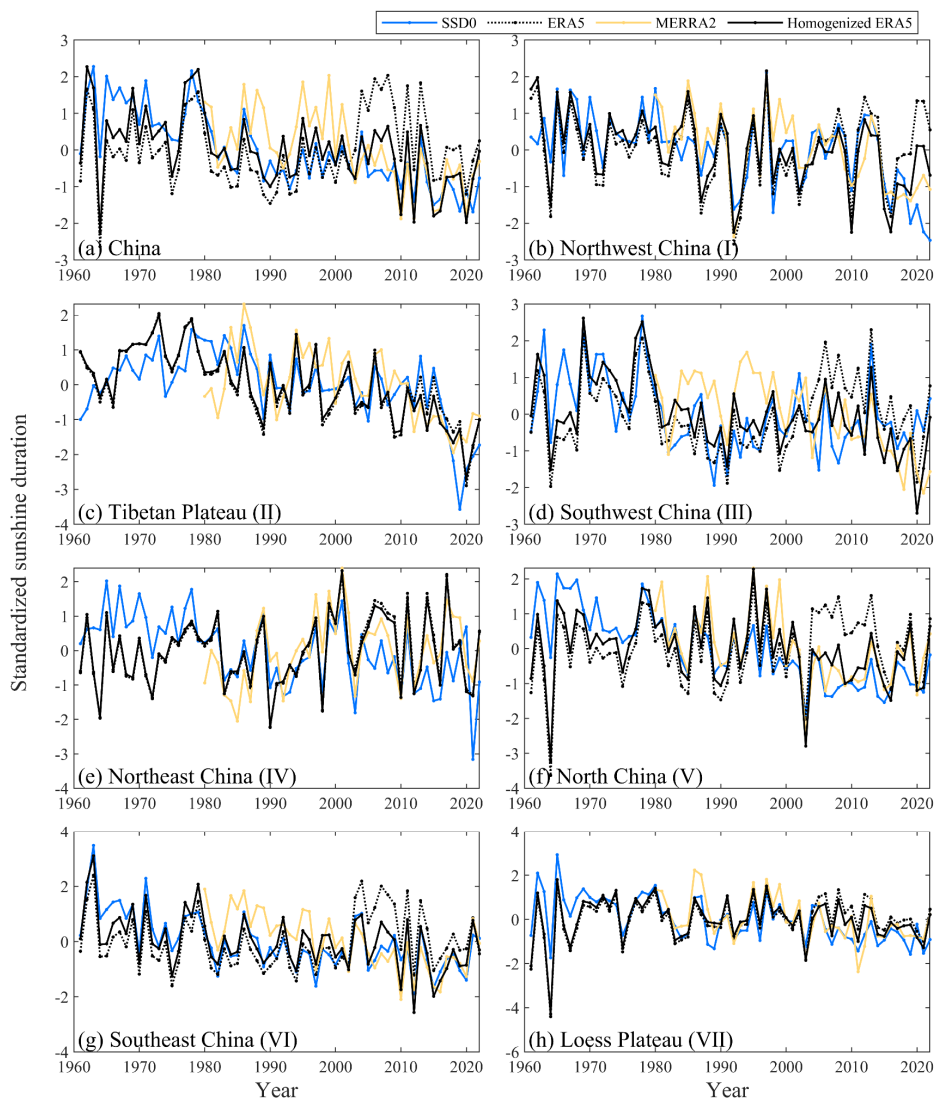
659

660 **Figure 3** Comparison of raw sunshine duration (Raw SSD, blue line, unit: hours·day⁻¹) with
661 the day0-type corrected sunshine duration (SSD0, red line, unit: hours·day⁻¹) at two example
662 stations in (a-c) Northeast China and (d-f) Northwest China, respectively. (a and d) QM
663 adjustments added to the raw SSD; (b and e) Daily time series of the raw SSD and SSD0; (c
664 and f) as in (b and e), but for their monthly SSD anomalies. The vertical grey lines indicate the
665 start and end dates of segments identified with the day0-type discontinuities.



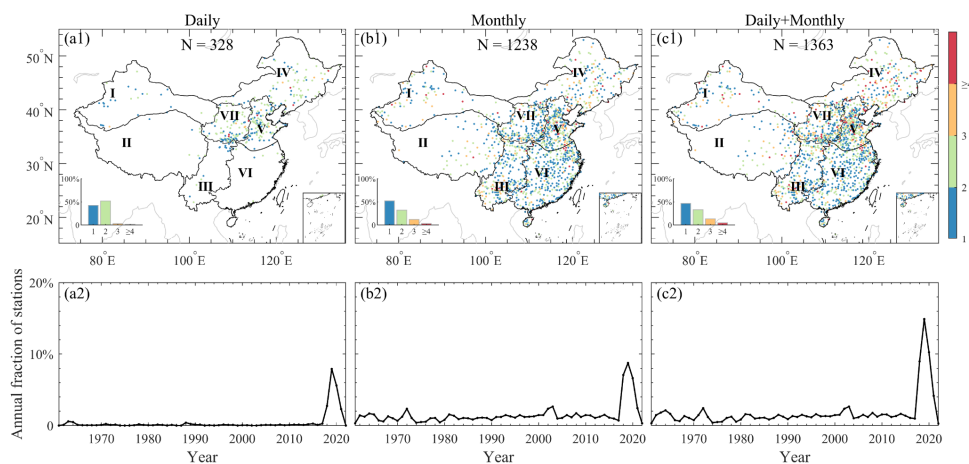
666

667 **Figure 4** Maps of the correlation coefficients of sunshine duration at daily, monthly and annual
668 time scales between the day0-type corrected observation (SSD0) and ERA5, MERRA2 as well
669 as homogenized ERA5.



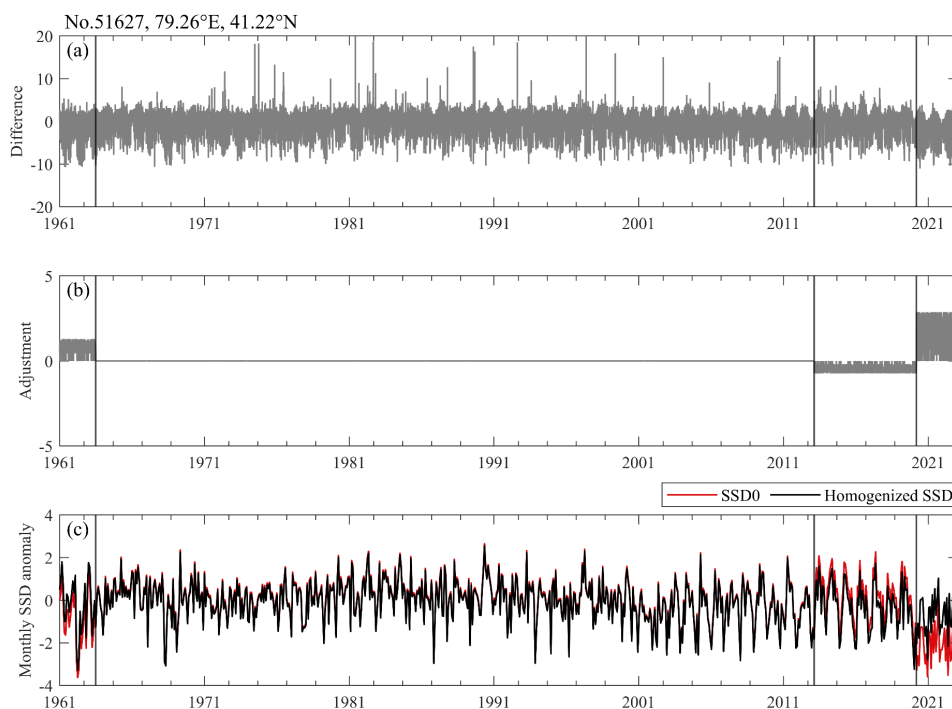
670

671 **Figure 5** Time series of the standardized sunshine duration (unit: 1) from the day0-type
672 corrected observation (SSD0, blue line), ERA5 (black-dotted line), MERRA2 (yellow line),
673 and homogenized ERA5 (black line) in (a) China and (b-h) its seven subregions.



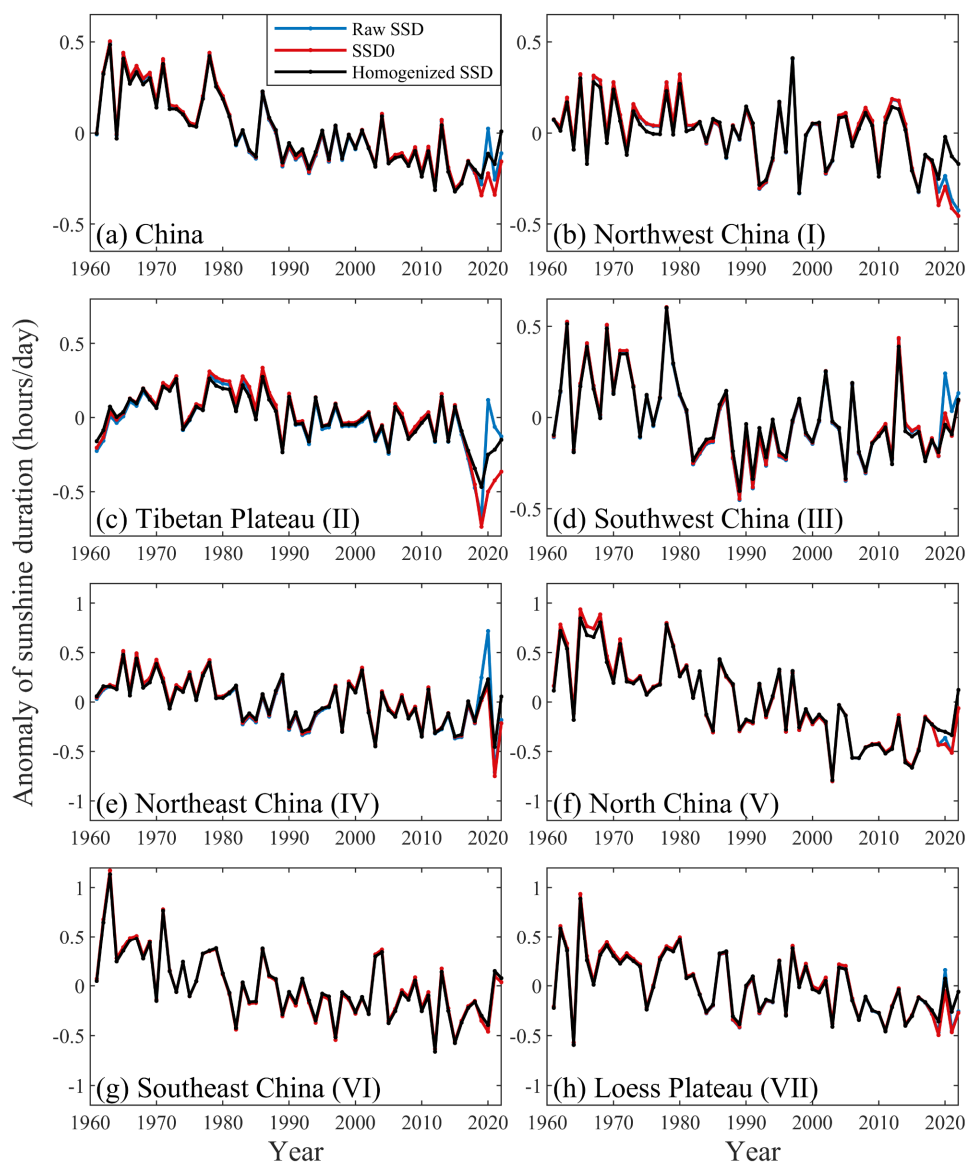
674

675 **Figure 6** (a1 and b1) Maps of the number of breakpoints detected in the daily variance and
676 monthly mean of the non-zero SSD0 series, respectively. (c1) Map of the number of
677 breakpoints merged from those in Figure 6a1 and 6b1. The total number (N) of stations with
678 one or more breakpoints from 1961 to 2022 is shown in each panel. (a2, b2, and c2) Annual
679 fraction (unit: %) of stations with the breakpoints from 1961 to 2022.



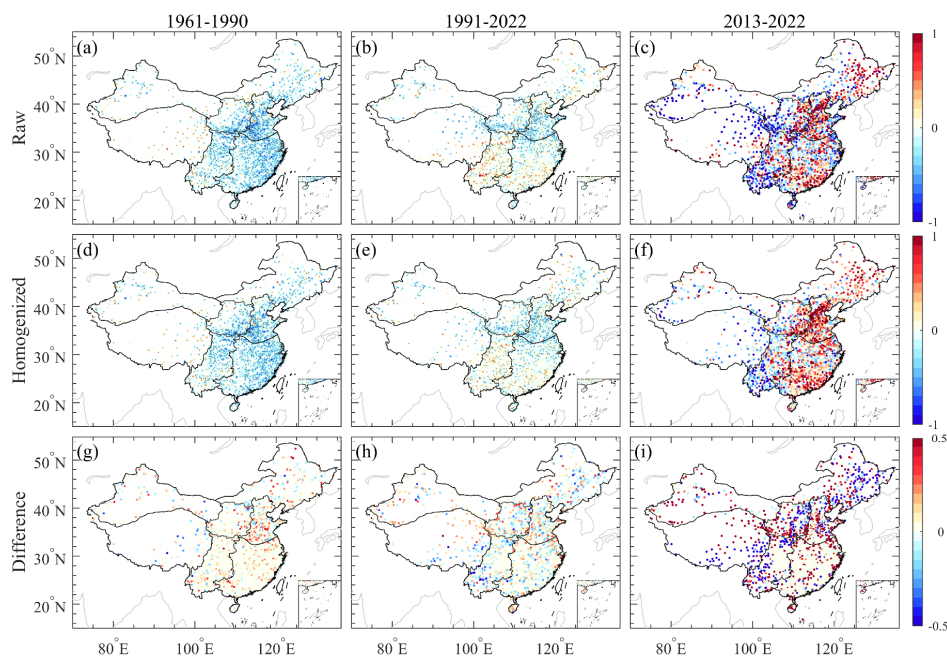
680

681 **Figure 7** Comparison of the day0-type corrected sunshine duration (SSD0, red line) before and
682 after homogenization (Homogenized SSD, black line) at an example Station No. 51627 in
683 Northwest China. (a) Daily SSD difference (unit: hours·day⁻¹) between the SSD0 and the
684 corrected ERA5 reference series; (b) QM adjustments added to the SSD0; (c) Monthly anomaly
685 series of the SSD0 (red line) and homogenized data (black line). The vertical lines indicate the
686 dates of the breakpoints detected.



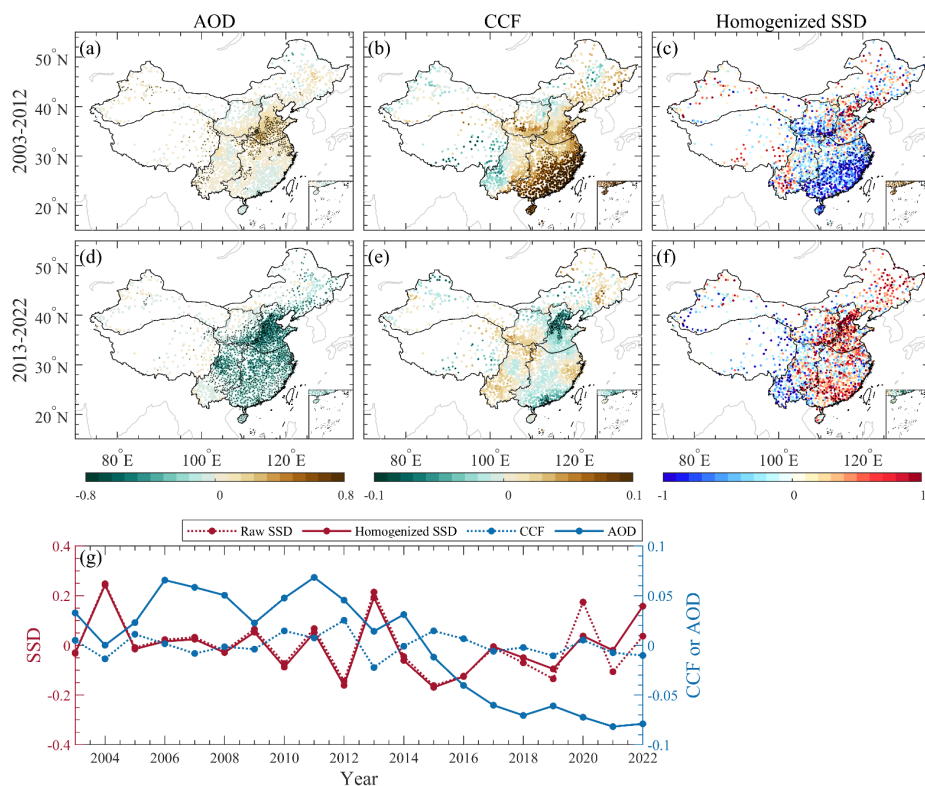
687

688 **Figure 8** Time series of raw sunshine duration (Raw SSD, blue line), the day0-type corrected
689 SSD0 (red line), and the homogenized SSD (black line) in (a) China and (b-h) its seven
690 subregions from 1961 to 2022. The anomaly is referenced to the average for the entire period.



691

692 **Figure 9** Maps of the decadal changes (unit: hours·day⁻¹/decade) in (a-c) raw sunshine duration,
693 (d-f) homogenized SSD, and (g-i) their difference over China during three periods of 1961-
694 1990, 1991-2022, and 2013-2022, respectively. Black dots superimposed on the colored circles
695 indicate a significance level of 0.10.



696

697 **Figure 10** (a-c) Maps of the decadal changes in aerosol optical depth (AOD, unit: 1/decade),
698 cloud cover fraction (CCF, unit: 1/decade), and homogenized sunshine duration (Homogenized
699 SSD, unit: hours·day⁻¹/decade) over China from 2003 to 2012. (d-f) Same as Figure 10a-10c,
700 but from 2013 to 2022. Black dots indicate a significance level of 0.10. (g) Time series of the
701 raw SSD (red dotted line), homogenized SSD (red solid line), CCF (blue dotted line) and AOD
702 (blue solid line) from 2003 to 2022.